

A numerical investigation of Matched Source Waveform Inversion applied to acoustic transmission data

William W. Symes¹, Huiyi Chen² and Susan E. Minkoff³

¹ *Department of Computational and Applied Mathematics, Rice University, Houston
TX 77251 USA*

² *Department of Mathematical Sciences, FO 35, University of Texas at Dallas,
Richardson, TX 75080 USA*

³ *Brookhaven National Laboratory, PO Box 5000, Upton, NY 11973-5000 USA*

ABSTRACT

Iterative inversion of seismic, ultrasonic, and other wave data by local gradient-based optimization of mean-square data prediction error (Full Waveform Inversion or FWI) can fail to converge to useful model estimates if started from an initial model predicting wave arrival times in error by more than half a wavelength (a phenomenon known as cycle skipping). Matched Source Waveform Inversion (MSWI) extends the wave propagation model by a filter that shifts predicted waves to fit observed data. The MSWI objective adds a penalty for deviation of this filter from the identity to the mean-square data misfit. The extension allows the inversion to make large model adjustments while maintaining data fit and so reduces the chances of local optimization iterates stagnating at non-informative model estimates. Theory suggests that MSWI applied to acoustic transmission data with single-arrival wavefronts may produce an estimate of refractive index similar to the result of travel time inversion, but without requiring explicit identification of travel times. Numerical experiments conform to this expectation, in that MSWI applied to single arrival transmission data gives reasonable model estimates in cases where FWI fails. This MSWI model can then be used to jump-start FWI for further refinement of the model. The addition of moderate amounts of noise (30%) does not negatively impact MSWI's ability to converge. However, MSWI applied to data with multiple arrivals is no longer theoretically equivalent to travel-time tomography and exhibits the same tendency to cycle-skip as does FWI.

INTRODUCTION

Matched Source Waveform Inversion (MSWI) (Huang and Symes, 2015; Huang et al., 2017) is a variant of Full Waveform Inversion (FWI) (Virieux and Operto, 2009), or

least-squares minimization of the misfit between observed and predicted propagating wave data. The large size of the computational domain for typical FWI problems means that efficient local (Newton-like) optimization methods offer the only practical solution approaches. However, such algorithms have a tendency to stagnate at sub-optimal model estimates, which fail to predict wave arrivals at correct times. Wave data is oscillatory, and the failure to predict correct arrival times manifests as matching of incorrect parts of the oscillatory wave data (“cycle-skipping”) (Virieux and Operto, 2009).

This paper reviews the theoretical basis of MSWI, describes a practical computational framework, and numerically illustrates the theory by applying MSWI to solve several synthetic acoustic inversion problems for cases in which least-squares FWI fails. The theory suggests that for data generated from smooth acoustic models with single-arrival wavefronts, approximate minimization of the MSWI objective via a modest number of local optimization iterations can produce an intermediate model that then allows iterative FWI to successfully approximate a global minimizer. We present several numerical experiments supporting this contention. We show other examples in which (1) MSWI produces a smooth initial estimate from which FWI succeeds, despite non-smooth features in the target model; and (2) MSWI produces an initial estimate from which FWI succeeds, despite the presence of significant coherent data noise; and (3) MSWI fails to produce a suitable initial model for FWI due to the presence of multiple arrival times between source and receiver points. In all of these examples, FWI fails due to cycle skipping when started from the same initial model as MSWI.

MSWI loosens the bond between predicted and observed data by interposing a filter, adapted to map the two datasets trace-by-trace. The MSWI objective function is a linear combination of the mean-square error between the observed data and the filtered predicted data and a quadratic penalty that vanishes when the filter is an impulse. This construction effectively relaxes the FWI data-fitting problem and permits local optimization methods to make large changes to the model and predicted data while maintaining fit of filtered predicted and observed data.

The theoretical justification for MSWI lies in its link to travel time tomography (Song, 1994; Symes, 1994; Huang and Symes, 2015; Huang et al., 2017; Symes, 2024). For smooth acoustic models producing simple wavefronts (single arrival times between sources and receivers), the MSWI objective function is proportional to a version of the travel time tomography objective, up to an error that decreases with increasing data frequency in time. Travel time tomography (minimization of the mean-square error between predicted and observed travel times) is commonly used to construct initial models for FWI (Bording et al., 1987; Sirgue and Pratt, 2004; Virieux and Operto, 2009). It is widely believed to be free of stationary points other than global minimizers, although theoretical support for this contention seems to be lacking. Thus we expect similar behaviour of the MSWI objective function, provided that the observed data is produced from a smooth model with single arrivals. Since matching

of arrival times (to within a half-wavelength or so) is the conventional criterion for successful initiation of FWI, we expect that an approximate minimizer of the MSWI objective function may be a good initial guess for iterative FWI. The theory also suggests that the MSWI-tomography link may fail for multi-arrival data.

MSWI in the form described here is mathematically equivalent to an *extended* formulation of the inverse problem, in which acoustic point sources are allowed to depend on the positions of receiving sensors, a non-physical expansion of the simulation domain. A number of other variants of FWI have been based on essentially the same extension of acoustic modeling (Song, 1994; Symes, 1994; Plessix, 2000; Luo and Sava, 2011; Li and Alkhalifah, 2021). In particular this extension is also the basis of Adaptive Waveform Inversion (AWI) (Warner and Guasch, 2016; Guasch et al., 2019; Warner et al., 2021; Guasch et al., 2020). MSWI is closely related to AWI but not identical. AWI includes a normalization of the adaptive filter, which makes the AWI objective function an even closer approximation to travel time mean square error than is MSWI, at least for transmitted wave data with a single arriving wavefront (Symes, 2024).

Huang et al. (2017) also present a numerical exploration of MSWI, illustrating some of the same major points made in this paper. However, their work differs in two key respects from that reported here. First, Huang et al. (2017) use frequency-domain simulation of acoustic wave motion, whereas we use time-domain methods. Second, and more important, we use a penalty function formulation of MSWI, whereas Huang et al. (2017) use a zero-weight limit of this penalty function as the objective (the relation between the two approaches is explained in the Theory section below). Our previous work on a single-trace analogue of MSWI (Symes et al., 2022; Chen et al., 2022) explored the potential benefits of the penalty approach, including the possibility of data noise estimation.

The next section describes versions of FWI and MSWI based on acoustic wave propagation and reviews the theoretical connection between MSWI and travel time inversion. The third section details the computational methods used to simulate acoustic data, apply local optimization to the objective functions, implement variable projection reduction of MSWI, and control smoothness of the estimated model via weighted norms in the domain of the simulation operator. In the main section of the paper we provide numerical examples that illustrate the theory. The final Discussion Section describes several additional topics for future work including penalty weight selection, inclusion of more complex physics, and other extension methods that may overcome FWI’s stagnation tendencies even with complex data kinematics.

THEORY

For all the experiments described in this paper, we assume acoustic wave propagation with isotropic point sources and receivers. The pressure and velocity fields $p(\mathbf{x}, t; \mathbf{x}_s)$, $\mathbf{v}(\mathbf{x}, t; \mathbf{x}_s)$ for the source location \mathbf{x}_s depend on the bulk modulus $\kappa(\mathbf{x})$, buoyancy β

(reciprocal of the density ρ), and source wavelet $w(t)$ through the acoustic system

$$\frac{\partial p}{\partial t} = -\kappa \nabla \cdot \mathbf{v} + \left(\int^t w \right) \delta(\mathbf{x} - \mathbf{x}_s);$$

$$\frac{\partial \mathbf{v}}{\partial t} = -\beta \nabla p; \quad (1)$$

$$p, \mathbf{v} = 0 \text{ for } t \ll 0. \quad (2)$$

The model vectors, $m = (\kappa, \rho)$, and the source wavelet, w , make up the domain of the forward map or *modeling operator* $F[m] = \{p(\mathbf{x}_r, t; \mathbf{x}_s)\}$, for specified source and receiver positions $\mathbf{x}_s, \mathbf{x}_r$ and recording time interval.

In the discussion that follows, the buoyancy, β , and the source wavelet, w , will be regarded as fixed, known parameters. Thus m is effectively the bulk modulus field κ . In practice, neither buoyancy nor source characteristics may be known precisely and instead should be added to the parameters to be determined by inversion.

FWI and the Weighted Gradient

In this setting FWI means: given buoyancy, source wavelet, and data traces, $d(\mathbf{x}_r, \cdot; \mathbf{x}_s)$, find a model, m , so that $F[m] \approx d$. The simplest version of FWI involves finding a model that minimizes the mean square error

$$J_{\text{FWI}}[m; d] = \frac{1}{2} \|F[m] - d\|^2 = \frac{1}{2} \sum_{\mathbf{x}_s, \mathbf{x}_r} \int dt |F[m](\mathbf{x}_r, t; \mathbf{x}_s) - d(\mathbf{x}_r, t; \mathbf{x}_s)|^2 \quad (3)$$

The integrals (or discrete approximations) are taken over the recording interval.

The approach to local optimization taken here (and in most work on FWI and related topics) is based on the gradient of the objective defined in equation 3:

$$g = \nabla J_{\text{FWI}}[m; d] = D_m(F[m])^T (F[m] - d). \quad (4)$$

In this formula, $D_m(F[m])$ is the derivative of $F[m]$ with respect to m . This gradient is the Euclidean (or L^2) gradient, that is, the vector g for which the Euclidean inner product

$$\langle g, \delta m \rangle = g^T \delta m \quad (5)$$

with any other vector δm gives the rate of change in the direction of that vector of J_{FWI} at m .

The theoretical basis for MSWI mentioned in the Introduction pertains to wave propagation through acoustic materials with model parameter fields (density, sound velocity, etc) which are smoothly varying in space. Most of the examples presented below are designed to explore aspects of this theoretical prediction: the search for an

optimal model (for either FWI or MSWI) should take place within a set of smooth models. In practice, wave measurements encompass finite ranges of temporal and spatial frequency, and “smooth” or “smoothly varying” means “slowly varying on the scale of spatial wavelength”. To ensure that estimated models remain smooth throughout the optimization process, we will penalize oscillation of the search vector. A *weighted inner product* (rather than the Euclidean inner product $\langle \cdot, \cdot \rangle$) in the space of models, defined by a weight operator W , provides a convenient device to apply such a penalty. W should be symmetric and positive definite. As is standard, we define the inner product $\langle \cdot, \cdot \rangle_W$ to be:

$$\langle g, \delta m \rangle_W = g^T W \delta m \quad (6)$$

Comparing the definitions 4, 5, and 6, one sees that the vector g_W for which $\langle g_W, \delta m \rangle_W$ gives the rate of change of J_{FWI} at m in the direction δm is

$$g_W = W^{-1} \nabla J_{\text{FWI}}[m; d] = W^{-1} D_m(F[m])^T (F[m] - d). \quad (7)$$

If W is chosen to greatly amplify components of the vector to which it is applied that oscillate on the wavelength scale and below, then those components of g_W must be suppressed relative to the corresponding components of g , hence g_W represents a non-oscillatory or smooth search direction. That is, the gradient with respect to the weighted inner product *smooths* the gradient 4 with respect to the Euclidean inner product. Note that only the inverse operator W^{-1} appears in the formula 7. The weight operator W itself is not needed. Therefore we can conveniently use weight operators W that are difficult to compute, so long as the inverses W^{-1} are easy to compute.

MSWI and Variable Projection

As mentioned earlier, application of local optimization methods directly to J_{FWI} tends to produce unsatisfactory model estimates. MSWI modifies the measure of distance between predicted and observed data by inserting an adaptive filter field u , with one filter per trace. Since both filters and data to which they are applied are defined only on finite time intervals, we introduce the *truncated filter operator* $K[u]$. This operator acts by extending both the filter and the input function to be zero outside of their intervals of definition. The resulting functions on the real line are convolved then truncated to the domain of the input. This operator is applied to the predicted data $F[m]$ to produce the filtered predicted data $K[u]F[m]$.

Note that the filtered predicted data may be viewed as the predicted data for an *extended source*, with the source wavelet at location \mathbf{x}_s replaced by $u(\mathbf{x}_r, \cdot; \mathbf{x}_s) * w(\cdot)$. That is, the adaptive filter construction is equivalent to allowing the source to depend on receiver position as well as source position - one source wavelet for each source-receiver pair. This construction is an extension of standard modeling in that the

domain (bulk modulus, buoyancy, wavelet) is larger than in the conventional formulation, and the standard and extended models are the same if the source wavelet is independent of receiver location. This *source-receiver extension* (Huang and Symes, 2015) is a key ingredient in a number of other papers on modifications of FWI as mentioned in the Introduction.

It is possible to make the error between filtered predicted data and observed data as small as one likes by choosing an appropriate filter field u , so this error by itself is useless for estimating the model. If, on the other hand, $u(\mathbf{x}_r, t; \mathbf{x}_s) = \delta(t)$, then the filtered predicted data is identical to the predicted data. Therefore, some penalty for divergence of the filter u from $\delta(t)$ needs to supplement the filtered prediction error. Similar to the works referenced in the Introduction, we use the mean-square of the filter scaled by a multiple of time t to measure deviation from δ . To stabilize the computation of the filter we also regularize via a multiple of the filter mean-square. These three terms together give the MSWI objective function:

$$J_{\alpha,\sigma}[m, u; d] = \frac{1}{2} (\|K[u]F[m] - d\|^2 + \alpha^2\|tu\|^2 + \sigma^2\|u\|^2). \quad (8)$$

The domain space (pairs of bulk modulus fields and adaptive filters) is very high-dimensional compared with the domain space for FWI (bulk modulus fields alone, in the present context). It is possible to optimize $J_{\alpha,\sigma}[m, u; d]$ by alternating updates of m and u (Li and Alkhalifah, 2021). However the *variable projection method* (Golub and Pereyra, 1973, 2003) is generally much more efficient than the alternating, or coordinate search, approach. In this instance, variable projection consists in minimizing $J_{\alpha,\sigma}[m, u; d]$ over u (a quadratic optimization) to produce an optimal choice $u_{\alpha,\sigma}[m; d]$. The reduced objective is

$$\tilde{J}_{\alpha,\sigma}[m; d] = \frac{1}{2} (\|K[u_{\alpha,\sigma}[m; d]]F[m] - d\|^2 + \alpha^2\|tu_{\alpha,\sigma}[m; d]\|^2 + \sigma^2\|u_{\alpha,\sigma}[m; d]\|^2). \quad (9)$$

Note that like the FWI objective, $\tilde{J}_{\alpha,\sigma}[m; d]$ depends only on m , with d as a parameter.

Relation to Travel Time Tomography

The first step in relating MSWI to travel time tomography is this simple observation about the small- α behaviour of the reduced MSWI objective $\tilde{J}_{\alpha,\sigma}$. Namely, that

$$\lim_{\alpha \rightarrow 0} \frac{1}{\alpha^2} (\tilde{J}_{\alpha,\sigma}[m; d] - \tilde{J}_{0,\sigma}[m; d]) = \|tu_{0,\sigma}[m; d]\|^2. \quad (10)$$

The right-hand side of equation 10 is itself a potential objective for a version of MSWI. In fact, it is the variant discussed by Huang and Symes (2015); Huang et al. (2017)). The related paper by Symes (2024) establishes the identity 10, and explains

the relationship between the RHS and the AWI objective function via an asymptotic analysis. High-frequency asymptotics are introduced by choosing the source wavelet, w , from a family $\{w_\lambda : 0 < \lambda \leq 1\}$, defined by

$$w_\lambda(t) = \frac{1}{\sqrt{\lambda}} w_1\left(\frac{t}{\lambda}\right), \quad 0 < \lambda \leq 1. \quad (11)$$

The wavelet w_1 is assumed to be smooth, of compact support (vanishing for large t), and to have zero mean. The scaled wavelets w_λ inherit these properties, and the dimensionless parameter λ is proportional to the RMS wavelength of w_λ . Note that the L^2 norm of w_λ is independent of λ .

Correspondingly, the theoretical basis for MSWI established in Symes (2024) really pertains to a λ -indexed family of models and data. Assume that

1. The regularization parameter σ^2 appearing in equations 8, 9, and 10 is proportional to the wavelength proxy parameter λ in definition 11 by a factor r :

$$\sigma^2 = r\lambda. \quad (12)$$

The units of r are $\text{pressure}^2 \times \text{time}^2$, so that definition 8 is dimensionally consistent. Call the corresponding family of modeling operators $\{F_\sigma\}$. These depend implicitly on λ .

2. Models $m = (\kappa, \beta)$ and $m^* = (\kappa^*, \beta)$ have the single-arrival property. Namely, for any source \mathbf{x}_s and receiver \mathbf{x}_r , there exists a single ray of geometric optics connecting the source and receiver, with travel times $\tau[m](\mathbf{x}_s, \mathbf{x}_r)$ and $\tau[m^*](\mathbf{x}_s, \mathbf{x}_r)$ respectively.
3. The data $d = d_\sigma$ is model-consistent (or zero noise), that is, $d_\sigma = F_\sigma[m^*]$.
4. Substitute F_σ for F , d_σ for d in the definitions 8 and 9.

Then for every source-receiver pair $(\mathbf{x}_s, \mathbf{x}_r)$, there exists $M[m, m^*, w_1](\mathbf{x}_s, \mathbf{x}_r) > 0$ so that

$$\|tu_{0,\sigma}[m; d_\sigma](\mathbf{x}_r, \cdot; \mathbf{x}_r)\| = \lambda^{-1/2} M[m, m^*, w_1](\mathbf{x}_s, \mathbf{x}_r) |\tau[m](\mathbf{x}_s, \mathbf{x}_r) - \tau[m^*](\mathbf{x}_s, \mathbf{x}_r)| + O(\lambda^{1/2}). \quad (13)$$

Thus the traveltim error at $(\mathbf{x}_s, \mathbf{x}_r)$ is equal to the L^2 norm of the t -scaled adaptive filter trace $tu_{0,\sigma}[m; d_\sigma](\mathbf{x}_r, \cdot; \mathbf{x}_s)$, scaled by $\lambda^{1/2}$ and a λ -independent factor. The error is proportional to λ (an RMS wavelength). From the limit relation 10 and the inequality 13,

$$\begin{aligned} & \lim_{\lambda \rightarrow 0} \lim_{\alpha \rightarrow 0} \frac{\lambda}{\alpha^2} (\tilde{J}_{\alpha,\sigma}[m; d_\sigma] - \tilde{J}_{0,\sigma}[m; d_\sigma]) \\ &= \sum_{\mathbf{x}_s, \mathbf{x}_r} M[m, m^*, w_1]^2(\mathbf{x}_s, \mathbf{x}_r) |\tau[m](\mathbf{x}_s, \mathbf{x}_r) - \tau[m^*](\mathbf{x}_s, \mathbf{x}_r)|^2. \end{aligned} \quad (14)$$

That is, in the $\lambda \rightarrow 0, \alpha \rightarrow 0$ limit, the reduced MSWI objective scaled by $\lambda/(\alpha^2)$ is proportional to a weighted version of the usual travel time tomography objective

As shown by Symes (2024), $\tilde{J}_{0,\sigma}$ is bounded independently of λ , so the second term in the left-hand side of equation 14 can be neglected for small λ (small σ). In the computations carried out below, we presume that for the choices made for $\sigma, \alpha, \tilde{J}_{\alpha,\sigma}$ can be regarded as a good approximation to the weighted mean square travel time error on the right-hand side of equation 14, hence as a suitable proxy for travel time inversion.

This relation is the one mentioned in the introduction. It does not show that the only stationary points are those of the mean square travel time error, even approximately, since the proportionality factor M depends on m . However if the scale factor $M[m, m^*, w_1]$ is relatively insensitive to changes in model, as is true if the source-receiver distance is well away from developing multiple arrivals, then any stationary point of $\tilde{J}_{\alpha,\sigma}$ is either close to a stationary point of $\|\tau - \tau^*\|^2$, or far from m^* . So we would expect minimization of $\tilde{J}_{\alpha,\sigma}$ to produce a model that closely matches the travel times inherent in the data ($\tau[m^*]$ in the notation used here), so long as the models involved are not close to generating multiple arrivals.

AWI adds one more feature, namely scaling *each trace* of the filter $u_{0,\sigma}[m; d](\mathbf{x}_r, \cdot; \mathbf{x}_s)$ by the reciprocal of its L^2 norm. This trace-by-trace normalization can be interpreted as a choice of weighted norm on the space of adaptive filters. It leads to a very similar relation to 13 for the AWI penalty function, but without the amplitude factors ($M[m, m^*, w_1]$, scaling by λ). Thus, the right-hand side of the AWI analogue of 14 is *just* the standard travel time tomography objective. See Symes (2024) for details.

Symes (2024) also shows that if energetic multiple arrivals are present in the data, for any reason, then cross-talk between travel time branches destroys the relation between MSWI (or AWI) and any version of the mean-square travel time error. The next sections of this paper will illustrate the success of MSWI for single-arrival data and its failure for data with multiple arrivals.

Computational Framework

The reduced adaptive filter $u_{\alpha,\sigma}[m; d]$ is the solution of the *normal equation*

$$(S[m]^T S[m] + \alpha^2 t^2 + \sigma^2 I)u = S[m]^T d, \quad (15)$$

in which $S[m]u = K[u]F[m]$. This positive definite symmetric linear system may be solved by various efficient numerical methods. Having computed $u_{\alpha,\sigma}[m; d]$ (hence the value of $\tilde{J}_{\alpha,\sigma}[m; d]$), its (Euclidean) gradient is given by

$$\nabla \tilde{J}_{\alpha,\sigma}[m; d] = D_m(F[m])^T K[u_{\alpha,\sigma}[m; d]]^T (K[u_{\alpha,\sigma}[m; d]]F[m] - d) \quad (16)$$

Apart from the appearance of the truncated filter operator $K[u_{\alpha,\sigma}[m; d]]$, this gradient is almost identical to the FWI gradient 4.

Use of a weighted norm in the model space goes exactly as before: with weight operator W , the weighted gradient is

$$\nabla_W \tilde{J}_{\alpha,\sigma}[m; d] = W^{-1} D_m(F[m])^T K[u_{\alpha,\sigma}[m; d]]^T (K[u_{\alpha,\sigma}[m; d]]F[m] - d). \quad (17)$$

The gradient (or weighted gradient), together with the function value, are the inputs to first-order optimization algorithms such as Steepest Descent and Limited-Memory Broyden-Fletcher-Goldfarb-Shanno iterations (Nocedal and Wright (1999)). Methods more closely related to Newton iteration require more involved computations (see for instance Kaufman (1975)).

NUMERICAL EXPERIMENTS

This section presents application of MSWI to inversion of 2D synthetic acoustic data. The computational experiments described here illustrate the capabilities and limitations of MSWI. In constructing these experiments we choose length, time, and frequency scales appropriate to crustal seismic exploration. With other scale choices these examples could become simplified representations of ultrasound tomography.

We emphasize that we do not attempt to illustrate the asymptotic relations discussed in the previous section directly. Instead, we make a choice of wavelet w and weight operator W (implicitly, a choice of wavelength and model smoothness) so that the computed data appears to be well-predicted by geometric acoustics, the foundation of the theoretical results reported above. We presume that this choice places our examples far enough into the asymptotic regime described above that the difference between $J_{\alpha,\sigma}$ and the weighted traveltime error $\lambda^{-1} \|M(\tau - \tau^*)\|^2$ is small. Hence minimizing the former produces small enough traveltime error to be a good initial guess for iterative FWI.

We begin with an example of a low-velocity circular lens anomaly with a vertical line of sources to the left of the anomaly and a vertical line of receivers to the right. This model produces single arrival data with clearly identifiable first arrivals shifted by well over a wavelength from those produced by a homogeneous bulk modulus model. Unsurprisingly, FWI starting from this homogeneous initial guess fails to recover the anomaly. We then use MSWI to generate a bulk modulus estimate. The final adaptive filter corresponding to this bulk modulus estimate is much closer to a band-limited, source-receiver-independent delta than is the adaptive filter for the initial homogeneous model. A subsequent FWI iteration beginning with the MSWI-generated model produces a near-perfect data fit as well as an adaptive filter which is a near-perfect band-limited delta.

We next illustrate failure of MSWI experimentally in the case of multi-arrival data. We use an oblate lens model, somewhat more focusing than the circular lens of the first example, and consider two source-receiver geometries. The first acquisition setup is the same as that for the circular lens experiment. In the second oblate lens experiment, the source and receiver lines are moved further apart. FWI starting from a homogeneous initial model fails in both cases. The data produced in the first acquisition case shows signal at multiple arrival times. However, the later arrivals have low enough energy that these multiarrivals are essentially treated as noise by MSWI. Hence MSWI produces a successful starting model for FWI. In the case of the second source-receiver geometry, the larger separation between sources and receivers leads to a more even division of energy between first and later arrivals, and MSWI fails to estimate a model predicting either set of arrival times, hence fails.

The theoretical justification of MSWI depends on the assumed smoothness of the model generating the observed data to be fit. Indeed, the choice of norm in the space of bulk modulus models forces the MSWI iteration to search through a suite of smooth models. The fourth example explores the effect of non-smoothness in the model generating the observed data. We use a variant of the “Camembert” model of Gauthier et al. (1986), the first published illustration of FWI failure through cycle skipping. We make implicit use of the observation of Barnier et al. (2023b,a), that extended inversion methods like MSWI allow independent control of temporal and spatial frequency. We estimate a smooth model via MSWI with model space norm that enforces smoothness, then use the resulting model as a starting point for FWI without enforcing smoothness. The result is an excellent data fit that reveals (some of) the sharp edges in the model.

Finally, all of the experiments described so far are “inverse crimes”. Namely, the data is noise-free and generated by the same simulation algorithm as used to drive the inversions (both MSWI and FWI). Given the close relation between MSWI and travel time inversion, the stability of the latter (Mukhometov, 1975; Tarikere and Zhou, 2024) suggests stability of the former. For the fifth example, we add roughly 30% coherent (model-generated) noise to the data of the first (circular lens) example. We show that FWI initialized on the MSWI-generated model is successful. In fact the algorithm picks out the arrivals corresponding to the noise-free data rather than matching the noise. This final inversion gives a good estimate of the RMS error, which in our usage is a synonym for “noise”.

Experimental setup

The experiments described below share a number of features which we detail in this subsection. Acoustic wave propagation is simulated via a staggered grid finite difference method (Virieux, 1986; Levander, 1988; Cohen, 2002) of order 2 in time and 8 in space. The time step is chosen so that the simulation results are stable, given upper

and lower bounds on the parameter fields, difference formulae, and spatial sampling. The discrete pressure field is output over the time range $0 < t < 5$ s with sample interval 0.008 s at externally specified receiver locations via piecewise linear interpolation in space and cubic spline interpolation in time. Isotropic point sources are added into the acoustic fields at each time step via the adjoints of these interpolation operations. (See Symes et al. (2011) for simulator details.)

The spatial domain for bulk modulus, buoyancy, gradients, etc, is a rectangular region of 8 km horizontally (“x”) and 4 km vertically (“z”), sampled on a 20×20 m grid. For all examples except the oblate lens with larger source-receiver separation and the non-smooth Camembert example, we use 181 receivers spaced 20 m apart, located on a vertical line at $x = 5000$ m, starting at a depth $z = 200$ m. Similarly, twenty isotropic point sources, spaced 150 m apart, occupy a line at $x = 3000$ m, starting at a depth of 500 m. Figure 1 shows the sources in green and the receivers in blue. For the second oblate lens example and the Camembert, source and receiver lines are moved further apart, to $x = 2000$ m and $x = 6000$ m respectively. (Other parameters remain the same.) Note that this geometry is a 2D cartoon of that used in cross-well seismic data acquisition. The source wavelets w are all trapezoidal bandpass filtered in the range [1.0, 2.5, 7.5, 12.5] with a median frequency of 5.875 Hz corresponding to a median wavelength of ≈ 340 m, and a shortest wavelength of 160 m. The wavelets are centered at $t = 1$ s.

The initial model m_0 for MSWI in all of the examples is homogeneous, with $\kappa = 4$ GPa, $\beta = 1 \text{ cm}^3/\text{g}$. As noted earlier, we regard β as fixed in this series of experiments, so mention of it will be suppressed. The corresponding data for 20 isotropic point sources at $x = 3000$ m and 181 point receivers at $x = 5000$ m is depicted in Figure 2. This figure shows pressure samples ranging between -0.005 to 0.005 GPa. (All similar plots have the same color scale.)

We apply a version of weighted LBFGS optimization (Nocedal and Wright, 1999) to the minimization of both J_{FWI} and $\tilde{J}_{\alpha,\sigma}$. The inverse weight operator (W^{-1} in formula 7) is a symmetrized 10-point moving average in both spatial directions, repeated once, except in the fourth example as discussed below. Recall that the weight operator itself is not required. The weighted gradient is computed via formula 4. The adjoint derivative $DF[m]^T$ is computed via the *adjoint state method* (Chavent and Lemmonier, 1974; Gauthier et al., 1986), with time reversal of the acoustic fields implemented via optimal checkpointing (Griewank, 1992, 2000; Symes, 2007). The LBFGS algorithm uses the weighted gradient (g_W , formula 7) to modify the search direction at each iteration, and the optimal step in this direction is approximated by a simple backtracking line search algorithm (Nocedal and Wright, 1999). The iteration terminates either when the gradient norm has fallen below 1% of its initial value or when a maximum number of iterations is reached.

While the initial model m_0 satisfies the upper and lower bound constraints of the staggered grid finite difference algorithm, later model updates may violate these bounds.

In fact, after only a few LBFGS iterations, bound violations occur in two of the examples discussed below. The finite difference implementation detects such bound violations and raises an exception, terminating the optimization. In effect, the finite difference parameter bounds add inequality constraints to the optimization of $\tilde{J}_{\alpha,\sigma}$. An optimization algorithm formulated for bound constraints, for example LBFGS-B (Zhu et al., 1997), could be used to avoid constraint violation and early termination in these examples. Since the bounds should be satisfied as strict inequalities at stationary points, we adopt a simpler approach. We reparameterize the wave velocity $c(\mathbf{x})$ by a dimensionless field $\gamma(\mathbf{x})$, via a logistic function

$$c(\mathbf{x}) = a + b \frac{\gamma(\mathbf{x})}{\sqrt{1 + \gamma(\mathbf{x})^2}}. \quad (18)$$

In the relation 18, the parameters a and b are chosen so that $c(\mathbf{x})$ lies strictly between the prescribed velocity bounds input to the staggered grid finite difference algorithm, regardless of the value of $\gamma(\mathbf{x})$. The bulk modulus is then computed via the relation $\kappa = \rho c^2$. This computation defines a map $\Gamma : \gamma \mapsto \kappa$, a diffeomorphism from the space of grid functions with the discretized L^2 norm onto the interior of the feasible set of gridded bulk moduli whose associated velocity fields satisfy the required bounds. In those cases in which LBFGS applied to $\tilde{J}_{\alpha,\sigma}$ results in bound violation, we apply LBFGS to $\tilde{J}_{\alpha,\sigma} \circ \Gamma$ instead. Since Γ is a diffeomorphism, stationary points of these two functions are in 1-1 correspondence, however application of LBFGS (or any other local optimization algorithm) to $\tilde{J}_{\alpha,\sigma} \circ \Gamma$ cannot produce a bound violation. Thus this simple change-of-variable device transforms a constrained optimization problem into an unconstrained problem, and is appropriate when the solution is expected to lie in the interior of the feasible set.

The MSWI objective $\tilde{J}_{\alpha,\sigma}$ requires choices of the parameters α and σ and solution of the normal equation 15. This system is far larger than is convenient to solve by any variant of Gaussian Elimination, even for our small 2D examples, so iterative methods are necessary. We choose the Conjugate Gradient (CG) method for solution of the normal equations (Daniels, 1967; Steihaug, 1983; Nocedal and Wright, 1999) and stop the iteration by monitoring the reduction in the normal residual (the gradient of $J_{\alpha,\sigma}[m, u; d]$ with respect to u). The reduction threshold ρ is thus another necessary input parameter. For all calculations in this paper, we choose $\rho = 0.01$. (Note that unlike α and σ , ρ is dimensionless.)

The choice of regularization weights (α and σ) is a widely studied topic. We mention some methods for this task in the Discussion Section. For the set of examples presented here, we take a simpler approach. In the asymptotic theory justifying MSWI, $\sigma > 0$ is roughly proportional to $\sqrt{\lambda}$. In this study, we explore neither the choice of λ nor the functional dependence of σ on λ . Instead we implicitly select λ , by choosing a single fixed wavelet, and assign $\sigma = 10^{-5}$, a value for which inner CG iterations converge relatively rapidly. We choose α by computing the adaptive filter $u_{\alpha,\sigma}[m_0; d]$ at the homogeneous model m_0 , for the data d used in the first example below, and for

$\alpha = 10^k$ for several values of k . . The largest such α that yields an RMS predicted data error ($\|S[m_0]u_{\alpha,\sigma}[m_0;d] - d\|$) less than $0.05\|d\|$ is $\alpha = 10^{-4}$. We use this value of α for all MSWI computations.

Recovering a circular lens

The target bulk modulus field (κ) for the first example is depicted in Figure 1. It contains an acoustic “lens” positioned in the center between $z = 1000$ – 3000 m depth. The background bulk modulus is 4 GPa. At the center of the lens, the bulk modulus is 2.4 GPa. As buoyancy (β) is spatially homogeneous at $1 \text{ cm}^3/g$, the background wave speed is 2000 m/s.

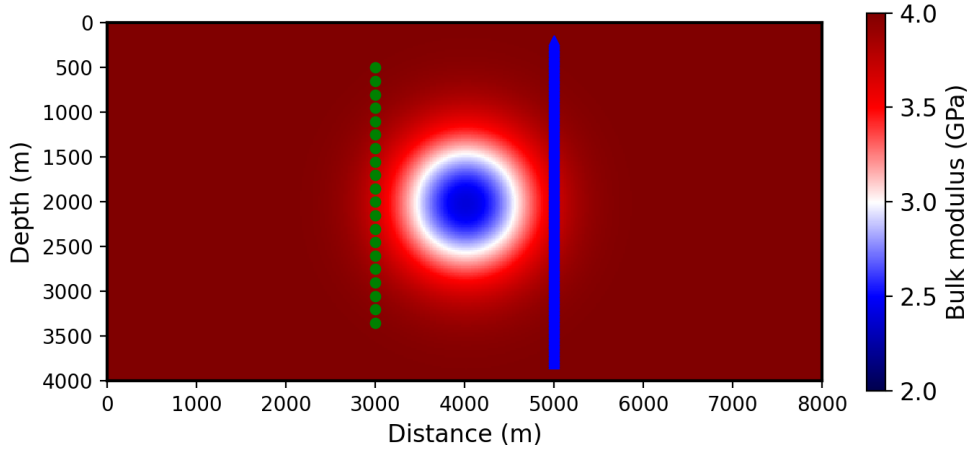


Figure 1: Lens model with 20 sources shown in green along a vertical line at $x = 3000$ m and 181 receivers shown in blue at $x = 5000$ m.

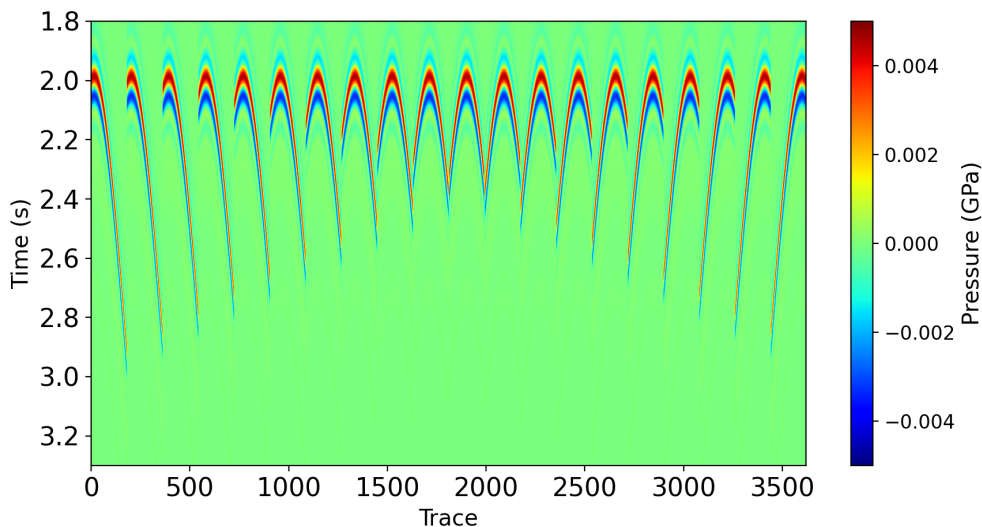


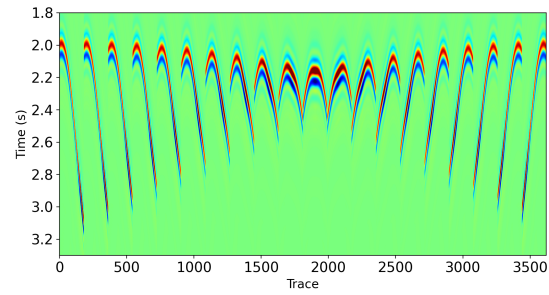
Figure 2: Data from the homogeneous initial model m_0 acquired using 20 sources located along a vertical line at $x = 3000$ m and 181 receivers at $x = 5000$ m.

The simulated data from this source-receiver configuration for the lens model appears in Figure 3a.

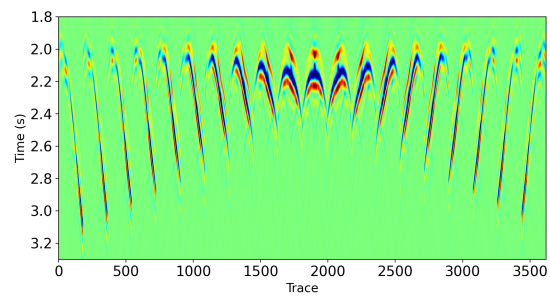
The value of $J_{\text{FWI}}[m_0, d] \approx 4.6$, and the initial gradient norm at m_0 is 2.1×10^{-3} . After 12 LBFGS steps the objective value has decreased to 2.4, and the gradient norm to $\approx 3.6 \times 10^{-4}$ (an order of magnitude). The final FWI inversion result appears in Figure 4.

While the reduction in the gradient norm indicates progress towards a stationary point, the RMS error $\|F[m] - d\|$ is still more than half of its initial value $\|F[m_0] - d\|$. Examination of the residual data (Figure 3b) shows that the approximate stationary point FWI produces does not predict arrival times correctly. In every example shown in this paper, straightforward application of FWI fails to produce a bulk modulus estimate that is even close to accurate. Therefore we will not display any of the FWI bulk modulus estimates or residual data in subsequent examples. The introduction of the adaptive filter in the formulation of MSWI is intended to overcome this failure to match arrival times. The filter u can shift events to their correct location in time, thus better fitting the data even for drastically incorrect models. The MSWI penalty term in the objective $J_{\alpha, \sigma}[m, u; d]$ measures the extent of the shift.

The use of a penalty term implies a choice of weight (α) as mentioned above. This example is the one on which we based the choice $\alpha = 10^{-4}$. We minimized $J_{\alpha, \sigma}[m_0, u; d]$ over u to identify an adaptive filter $u_{\alpha, \sigma}[m_0; d]$. As α increases, the MSWI fit error $\|S[m_0]u_{\alpha, \sigma}[m_0; d] - d\|$ at this minimizer increases (and the penalty $\|tu_{\alpha, \sigma}[m_0; d]\|$ de-



(a)



(b)

Figure 3: (a) Data for circular lens model shown in Figure (1). (b) FWI residual (difference between data predicted from the model shown in Figure 4 and target data shown in Figure 3a). Note the failure to match arrival times of the later signal, leading to large amplitudes in the central part of the display.

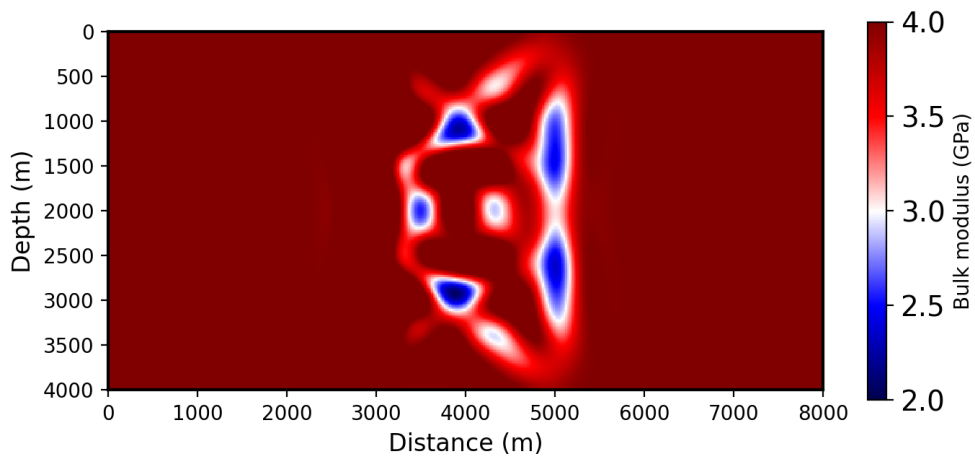


Figure 4: Bulk modulus produced by minimizing the FWI objective function given in Equation 3 using 12 LBFGS iterations. The data is shown in Figure 3a.

creases). We choose α just small enough to obtain an RMS error under 5% of the data norm $\|d\|$. The resulting filter $u_{\alpha,\sigma}[m_0;d]$ is shown in Figure 6a. It exhibits a lot of energy at non-zero times, as is necessary to move the events in data computed from the initial model m_0 (Figure 2) to match those in the target data (Figure 3a).

Throughout the following discussion, we will use the apparent dispersion of energy away from $t = 0$ shown by computed adaptive filters to judge the quality of inversions. All plots of adaptive filters in this paper use the same time range $[-0.4, 0.4]$ s, amplitude range $[-0.02, 0.02]$, and color scale as in Figure 6a.

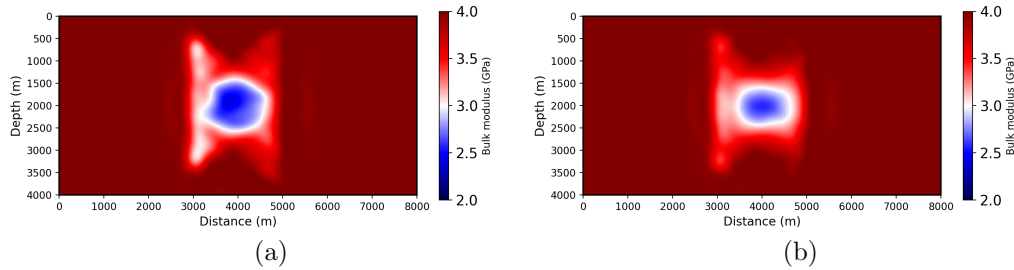


Figure 5: (a) Bulk modulus produced by 12 LBFGS steps to minimize the reduced MSWI objective given in Equation 9, using the data shown in Figure 3a. (b) Bulk modulus produced by 12 LBFGS steps to minimize the FWI objective 3, using the data shown in 3a, and starting at the MSWI result shown in Figure 5a. The gradient norm has been reduced by 2 orders of magnitude.

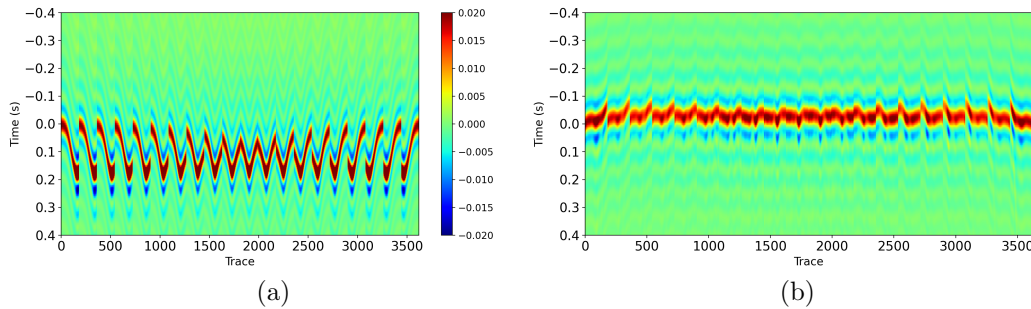


Figure 6: (a) Adaptive filter to match initial model data (Figure 2) to circular lens data (Figure 3a). Note considerable energy dispersion away from $t = 0$. (b) Adaptive filter to match data computed from the MSWI model (Figure 5a) to circular lens data (Figure 3a). Note that there is considerably less energy away from $t = 0$ than we see in the filter (Figure 6a) that matches data from the homogeneous model.

Next we minimize the reduced MSWI objective $\tilde{J}_{\alpha,\sigma}$ using LBFGS. The initial bulk modulus field is once again homogeneous at 4 GPa. The initial value of the reduced MSWI objective is $\approx 1.49 \times 10^{-2}$, and the initial gradient norm is $\approx 2.2 \times 10^{-5}$. After 12 LBFGS iterations, the objective value has decreased to $\approx 2.80 \times 10^{-3}$ (a factor of

5.3). The gradient norm is $\approx 1.3 \times 10^{-6}$, a reduction of one order of magnitude. The resulting bulk modulus is shown in Figure 5a.

The final adaptive filter is shown in Figure 6b. Note that energy in the filter has migrated towards $t = 0$ compared to the adaptive filter (shown in Figure 6a) from the homogeneous initial model. The majority of the energy is within an apparent half-wavelength of $t = 0$, suggesting that the MSWI estimate of bulk modulus (Figure 5a) may be an adequate initial estimate for a successful FWI.

Starting from the MSWI inversion result shown in Figure 5a, we minimize the FWI objective function using 12 iterations of LBFGS. The initial FWI objective value is ≈ 4.6 , and the initial gradient norm is $\approx 2.0 \times 10^{-2}$. After 12 steps of LBFGS, the prescribed reduction (10^{-2}) of the gradient norm is achieved, and the objective value has decreased to $\approx 2.4 \times 10^{-2}$. The resulting bulk modulus field is depicted in Figure 5b. The data is fit to within roughly 7% relative RMS error, and the residual (not shown) is almost invisible if plotted on the same scale as the data shown in Figure 3a. Thus the combination of MSWI starting from the homogeneous initial model, followed by FWI starting from the MSWI-estimated model, results in a quite precise data fit, far more accurate than that obtained by FWI alone.

Oblate lens: single vs. multiple arrivals

Our next two examples use a more refractive lens model which is no longer circular but instead is extended horizontally, placed somewhat deeper vertically, and has a minimum bulk modulus of 2 GPa in the center (see Figure 7.) As is the case with the circular lens, this oblate lens is smooth enough that the predicted data (Figure 8) appears to be well-approximated by geometric acoustics.

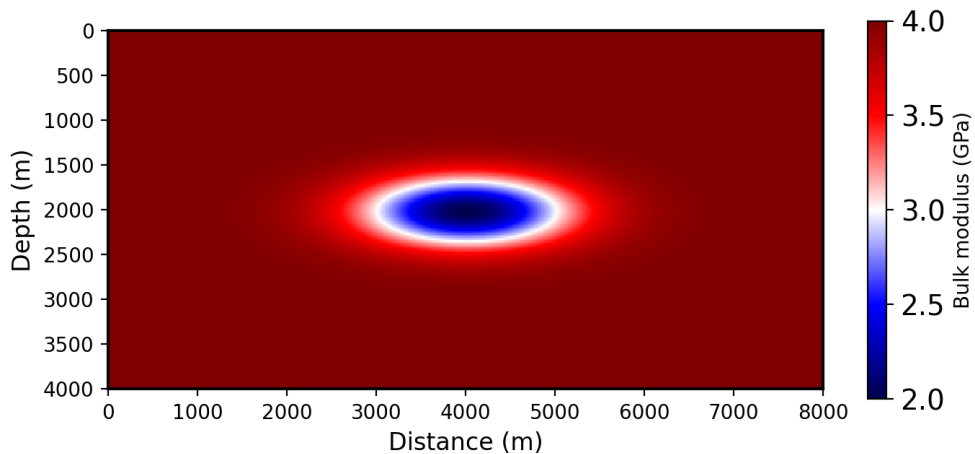


Figure 7: Oblate lens model.

The first example using this model has exactly the same acquisition geometry as was used in the circular lens example, namely, 20 sources in a vertical line at $x = 3000$ m, and 181 receivers at $x = 5000$ m with the same spacing as described in the previous section. The data is shown in Figure 8. The stronger refraction of this model results in a visible triplication at the center of the source-receiver line, and in fact in all parts of the data, although the smearing effect of finite bandwidth obscures this detail in several places. Hence most of the data can be (just!) regarded as exhibiting a single arrival on an identifiable wavefront.

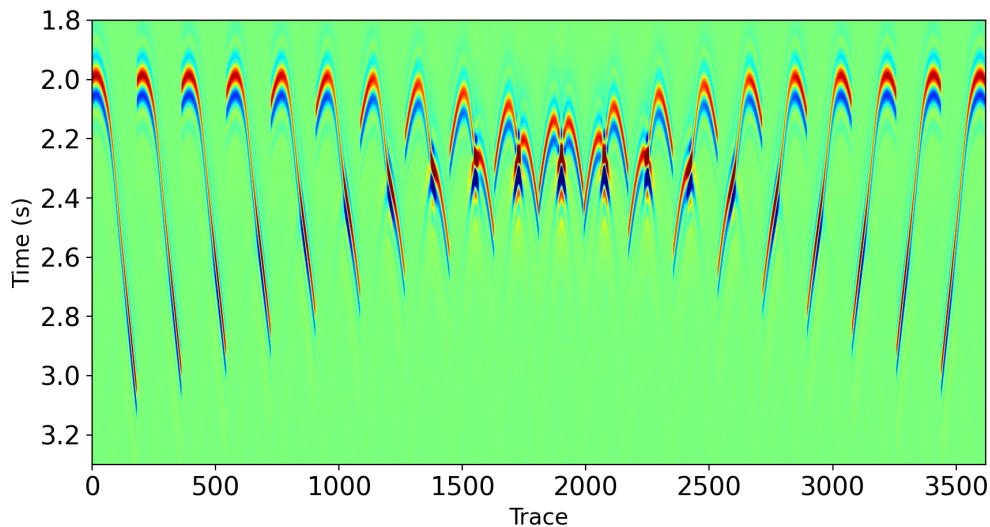


Figure 8: Data generated from the model shown in Figure 7 and the same source-receiver geometry as for the circular lens data.

As already mentioned, FWI initiated from the homogeneous model fails for all examples shown in this paper. Application of LBFGS to the MSWI objective (with the same parameters as in the previous example) results in the model depicted in Figure 9a and reduces the objective value and gradient to roughly 18% and 7% of their initial values respectively.

The change in adaptive filters between the homogenous initial model and the MSWI inversion is shown in Figures 10a and 10b. The reduction in energy dispersion is evident. The adaptive filter appears to have the bulk of its energy within a half-wavelength of $t = 0$, making the MSWI inversion result a plausible initial estimate for FWI. We applied twelve LBFGS iterations to the FWI objective function using the data shown in Figure 8. The inversion starts from the final MSWI model shown in Figure 9a. Figure 9b shows the final model recovered by FWI. The objective function decreased to 1% of its initial value. Thus in this example, as in the first example, iterative LBFGS minimization of the MSWI objective with a modest number of iterations produces a satisfactory initial model for FWI inversion.

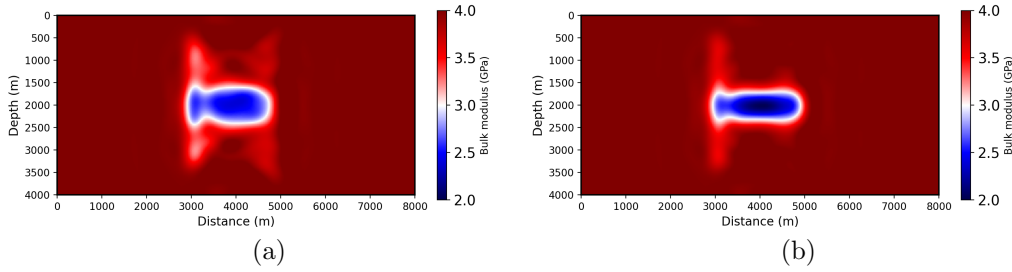


Figure 9: (a) Result of 12 LBFGS iterations applied to the MSWI objective function and the data shown in Figure 8 starting from the homogeneous model. (b) Bulk modulus produced by 12 LBFGS steps applied to the FWI objective using the data shown in 8 and starting at the approximate MSWI minimizer shown in Figure 9a.

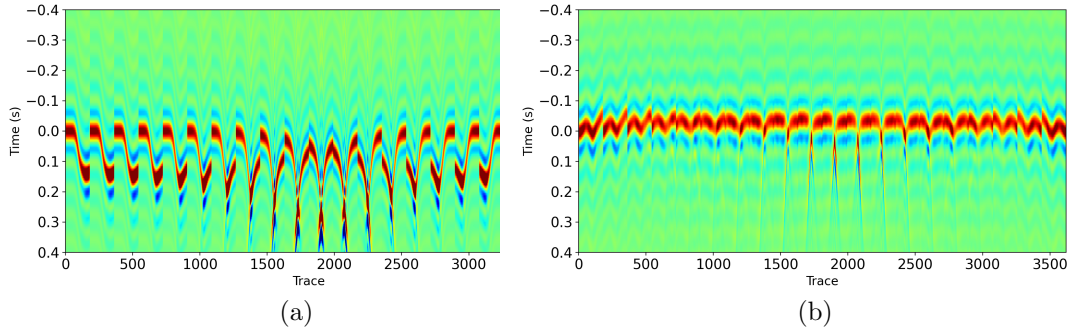


Figure 10: (a) Adaptive filter estimate starting the inversion at a homogeneous initial model and fitting the data in Figure 8. (b) Adaptive filter estimate from MSWI inversion result shown in Figure 9a.

The second example based on the target model in Figure 7 differs from the first *only* in that the sources and receivers have been moved 2 km further apart. The sources now lie on the line $x = 2000$ m, and the receivers are at $x = 6000$ m. All other aspects of data generation are the same. The resulting data is shown in Figure 11. Notice that this increase in offset between sources and receivers has allowed distinct energetic later arrivals to appear in the data. As before, we compute the adaptive filter required to produce the data of Figure 11 from the corresponding homogeneous medium data (Figure 2). This filter, displayed in 13a, shows that for most traces, two or more major energy peaks appear in the adaptive filter, forced by the need to match multiple energy peaks in the target data with the single energy peak in the homogeneous medium data.

This optimization appears to be more difficult. Because the reduction in MSWI gradient and objective function values achieved in 12 LBFGS iterations is not as great as was the case in the two previous examples, we perform 25 additional LBFGS

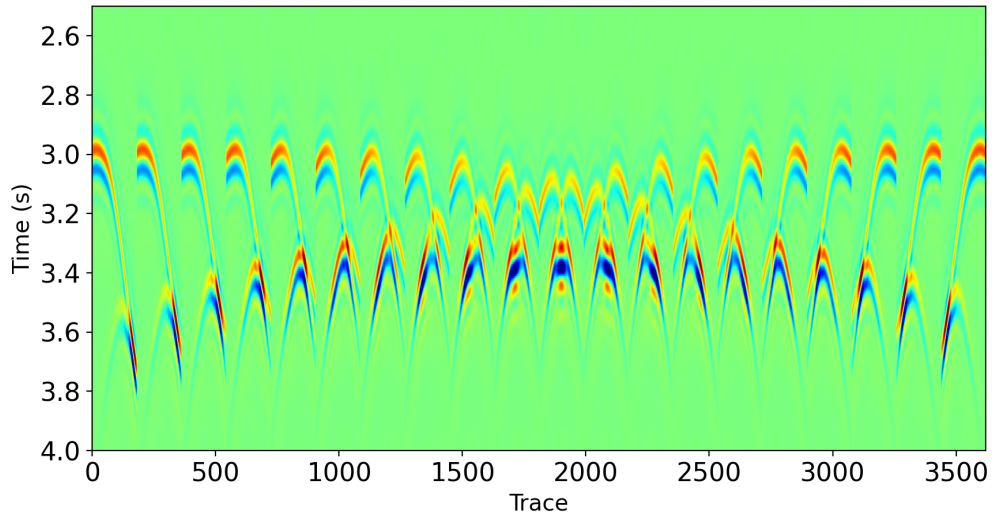


Figure 11: Data generated using the same inputs as in Figure 8, but with sources moved to $x = 2000$ m and receivers to $x = 6000$ m.

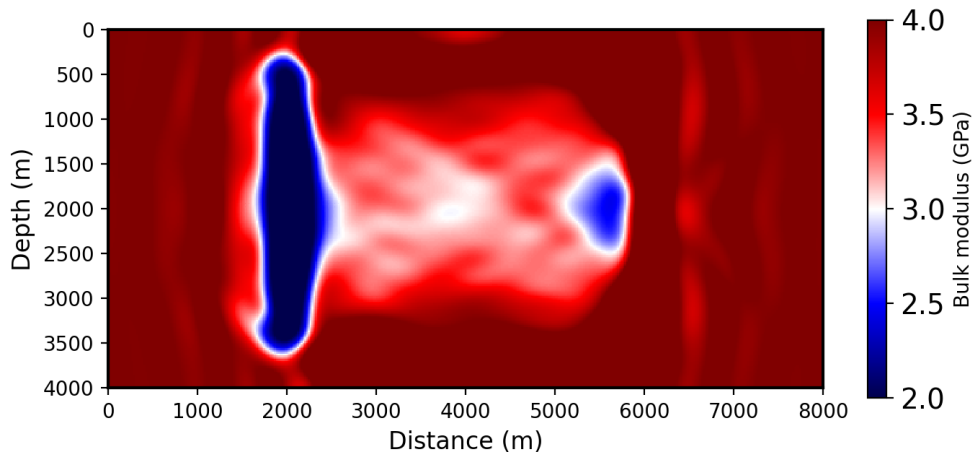


Figure 12: Result of 37 LBFGS iterations applied to the MSWI objective function for the data in Figure 11 starting from the homogeneous initial model.

iterations. The final objective value obtained after 37 LBFGS steps is roughly 7% of the initial objective value, and the gradient norm is approximately 4% of its initial value. While these norm decreases suggest a reasonably successful optimization, the approximate minimizer (Figure 12) does not at all resemble the target bulk modulus (Figure 7). The adaptive filter derived as a by-product of the MSWI minimization (Figure 13b) is no more focused at $t = 0$ than is the filter for homogeneous medium data (Figure 13a).

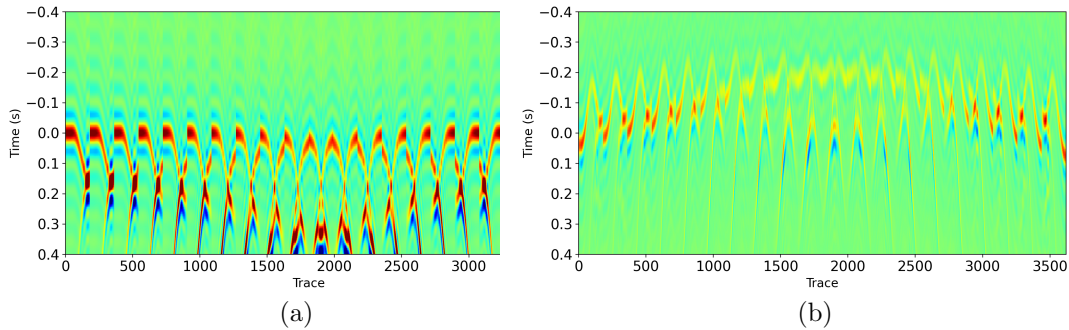


Figure 13: (a) Adaptive filter required to produce the data of Figure 11 from corresponding homogeneous medium data (Figure 2). (b) Adaptive filter estimate for MSWI inversion shown in Figure 12.

The model shown in Figure 12 does not appear to be a good initial estimate for FWI, and indeed it is not. Applying 25 LBFGS iterations to the FWI objective function starting from the MSWI model produces a reduction of the gradient norm to 3.5% of its initial value, thus an approximate stationary point. However the value of the RMS fit error has only decreased by a couple of percent. Since the data fit remains unsatisfactory, it is not surprising that the resulting bulk modulus estimate (not shown) is no better than the MSWI estimate (Figure 12).

This pair of examples based on the oblate lens model illustrate the behaviour of MSWI described in the *Theory Section*. The data in the first example (Figure 8) shows clear signs of caustic formation, but the amount of energy in later arrivals is small. Thus MSWI treats the data as single arrivals plus noise and delivers a model that largely matches the dominant first arrival times. The second example in the pair (see the data in Figure 11) distributes energy much more evenly between first and later arrivals, and MSWI fails to produce a useful model estimate.

Recovering a Camembert: effect of non-smoothness

The justification for MSWI relies on geometric asymptotics. The previous examples involve the recovery of a smooth bulk modulus model. To explore the implications of model non-smoothness - a common aspect of prototypical mechanical parameter distributions in the earth, the human body, and other potential wave imaging arenas - we apply the methodology developed above to a variant of a model introduced in one of the the first important papers on FWI, Gauthier et al. (1986). This model, shown in Figure 14, features a circular inclusion inside of which the bulk modulus is 20% higher than in the surrounding. (From its appearance in perspective plot, this model has come to be called the Camembert.) The geometry of sources and receivers is the

same as in last (third) example. The corresponding data (Figure 15) differs from that shown in Figure 8 in that only a single arrival is apparent. Indeed, the Camembert is a defocusing lens, rather than a focusing lens as in the previous examples, and does not generate multiple arrival times.

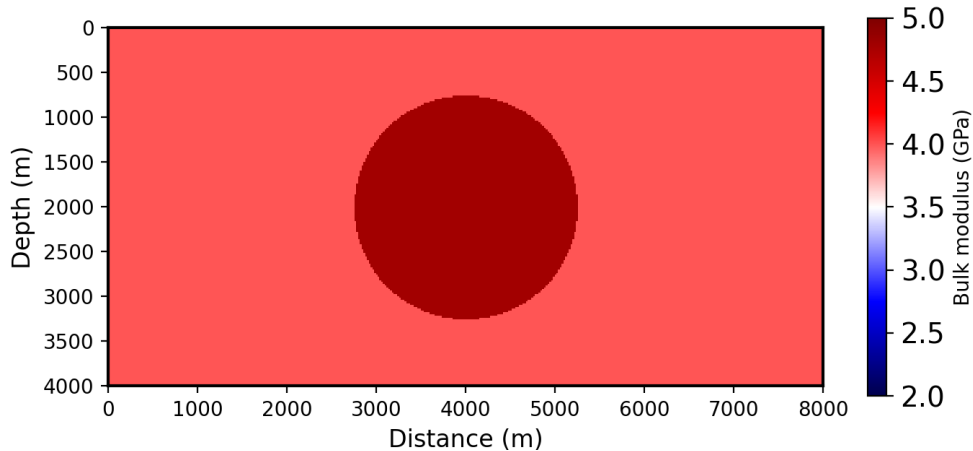


Figure 14: A model resembling the Camembert of Gauthier et al. (1986). Diameter of circular inclusion = 2500 m, approximately 8 wavelengths at median frequency. Interior value (4.8 GPa) is 20% above exterior (4.0 GPa).

Figure 17a shows the adaptive filter needed to match the data displayed in Figure 15 to the homogeneous medium data (Figure 2). The expected time lag of about 0.1 s is evident.

As has been true for all of the examples shown in this section, iterative FWI starting at the homogeneous background model fails to generate a significant improvement in data fit with a modest number of iterations. On the other hand, 12 LBFGS iterations applied to the MSWI objective function, also starting at the homogeneous background model, yields the estimated bulk modulus field shown in Figure 16, which resembles a smoothed version of the target. It is smoothed because we use the same inverse weight operator in the bulk modulus model space (10 point smoothing in both directions, repeated once) as in the previous examples. The adaptive filter returned at the final MSWI model (Figure 17b) has greatly reduced the apparent time shift.

To accommodate the non-smooth nature of the target model in this example, we use an idea articulated most clearly by Barnier et al. (2023b). Namely, for iterative inversion of wave data, the spatial frequency content of the trial models can be manipulated independently of the temporal frequency content of the data. The low spatial frequency components of trial models largely control the arrival times in predicted data, so it is natural to focus the inversion on them first. The previous examples have been based on smooth (low spatial frequency) target models, so determination of the low spatial frequency components was the whole story. Our version of the Camem-

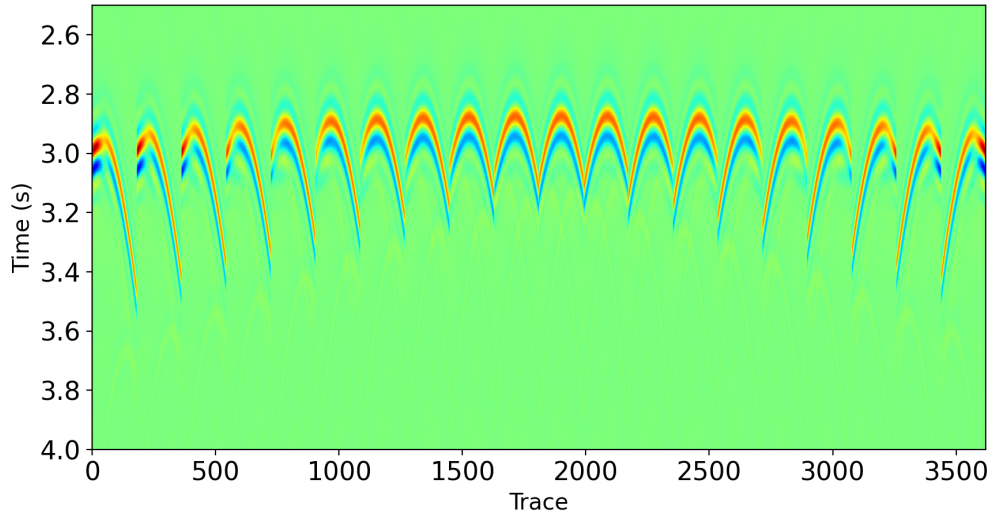


Figure 15: Data generated using the Camembert model with the same source-receiver geometry as in Figure 11: 20 sources located at $x = 2000$ m, spaced 150 m apart, starting at $z = 500$ m; 181 receivers located at $x = 6000$ m, spaced 20 m apart, starting at $z = 200$ m.

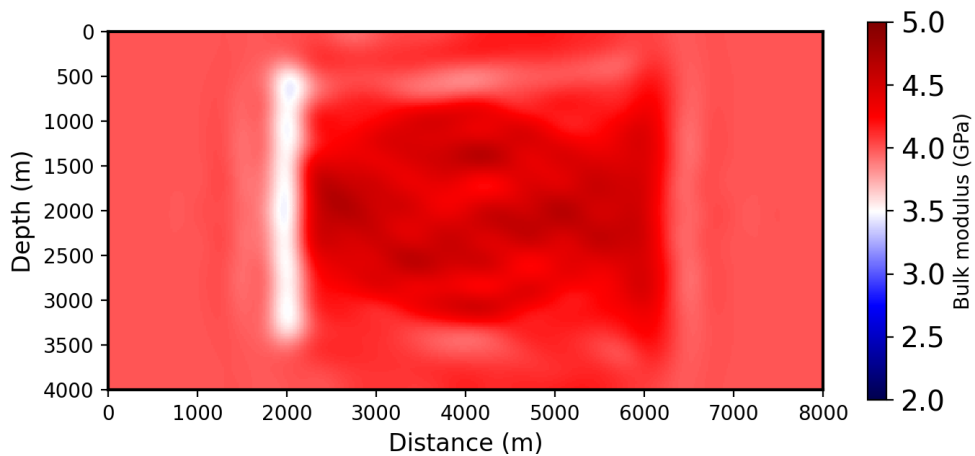


Figure 16: Result of 12 MSWI iterations applied to the data in Figure 15 starting from the homogeneous initial model.

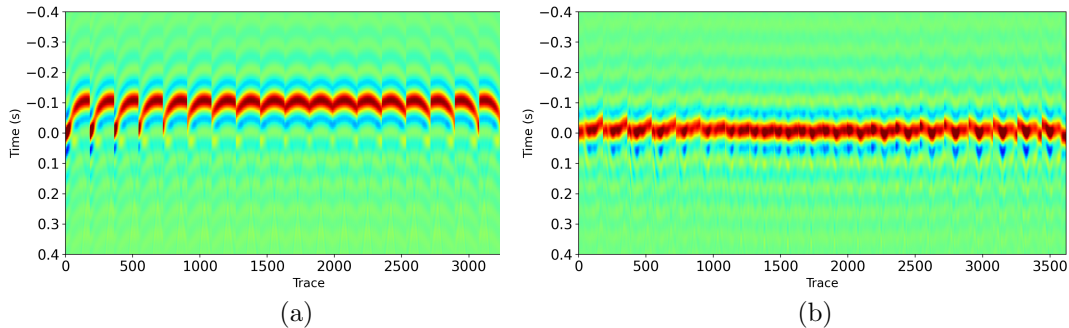


Figure 17: (a) Adaptive filter required to produce the data of Figure 15 from corresponding homogeneous medium data (Figure 2). (b) Adaptive filter estimate for MSWI inversion shown in Figure 16.

bert has high spatial frequency content. Rather than update the spatial frequency content during the extended inversion, as do Barnier et al. (2023b), we observe that the extended (MSWI) inversion has produced a kinematically accurate model, and update spatial frequency content during FWI (as pointed out above, effectively the $\alpha \rightarrow \infty$ limit of MSWI). Figure 18 shows the result of 12 LBFGS iterations applied to the FWI objective, starting with the MSWI-estimated model in Figure 16, and with the same inverse weight operator as before, followed by 25 iterations of LBFGS with a “hi-res” inverse weight operator (2 point moving average in both directions, repeated once). The final RMS error obtained is 1.4 % of the RMS error between the initial (homogeneous medium) predicted data (Figure 2) and the target data (Figure 15). The apparent spatial resolution is much higher in the vertical direction than in the horizontal direction (an artifact of the source-receiver geometry). The data is much more sensitive to the change in travel time across the top and bottom edges of the Camembert than to those across the left and right edges.

Data with Additive Noise

Seismic data contains substantial noise. Human activities such as road traffic and construction, and natural sources such as rivers, wind, and ocean waves can introduce noise in the data (Shearer, 2009). Medical ultrasonics data often exhibits speckle noise (Kavand and Bekrani, 2024). Finally, real world data are necessarily noisy because the underlying account of the physics is always simplified and hence incomplete. To test that our conclusions about MSWI are robust against the addition of modest amounts of noise, we present one example which includes 32% (RMS) added noise.

The example we describe in this subsection uses the target bulk modulus shown in Figure 1. We generate noise by adding uniformly distributed random numbers (from

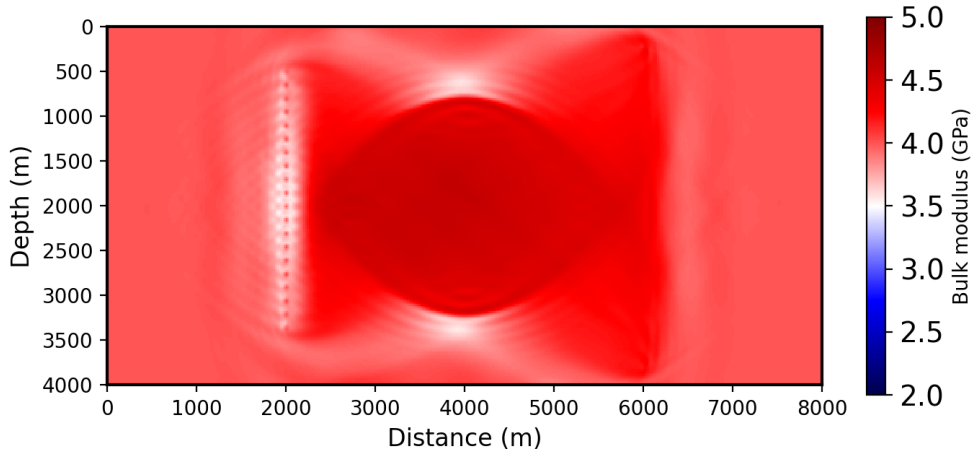


Figure 18: “Hi-res” bulk modulus produced by (1) 12 steps of LBFGS applied to MSWI objective, with (10 point moving average in both directions) inverse weight operator on bulk modulus followed by (2) 25 additional LBFGS steps, with (2 point moving average) inverse weight operator.

$[-1, 1]$ with mean zero and variance of $1/3$) to the homogeneous bulk modulus. The wave solution using this noisy model (and the same wavelet and buoyancy as in the circular lens experiment) is then added to the data shown in Figure 3a to create the data for our experiments. In this example, we display single shot gathers in order to show clearly the effect of the additive noise. The shot gather with source depth $z = 2000$ m appears in Figure 19.

We minimize the objective function $J_{\alpha, \sigma}[m_0, u; d]$ with respect to u starting from data shown in Figure 2. The resulting adaptive filter $u_{\alpha, \sigma}[m_0; d]$ is shown in Figure 21a. The initial value of the reduced MSWI objective is $\approx 3.96 \times 10^{-2}$, and the initial gradient norm is $\approx 9.1 \times 10^{-5}$. After 12 iterations of LBFGS, the MSWI objective value has decreased to $\approx 2.28 \times 10^{-3}$, and the norm of the gradient is $\approx 9.1 \times 10^{-6}$. The resulting bulk modulus is shown in Figure 20a, and the final adaptive filter is shown in Figure 21b. Finally, starting from the MSWI estimated bulk modulus shown in Figure 20a, we performed 12 more iterations of LBFGS with the FWI objective function. The FWI objective value starts at ≈ 9.37 and decreases to $\approx 2.87 \times 10^{-1}$. The resulting bulk modulus field is shown in Figure 20b.

DISCUSSION

In this section we will discuss some outstanding issues for the future including: the character of the FWI result, the choice of parameters in the definition of the MSWI objective, and the application of MSWI to inverse problems defined by other types

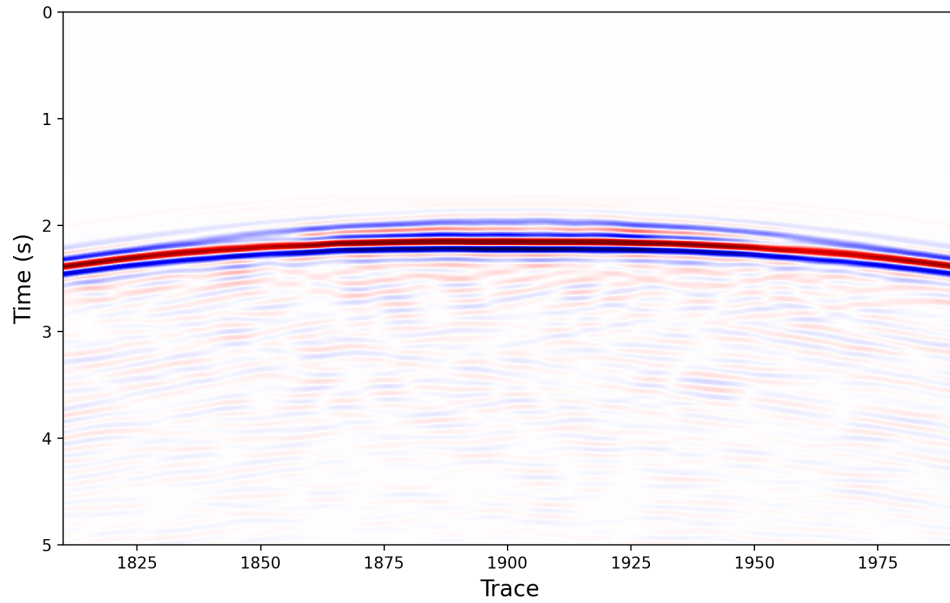


Figure 19: Data for the circular lens model (Figure 1) with approximately 32% added noise. While there are 20 sources at $x = 3000$ m, here we show a representative set of data from one shot at depth $z = 2000$ m.

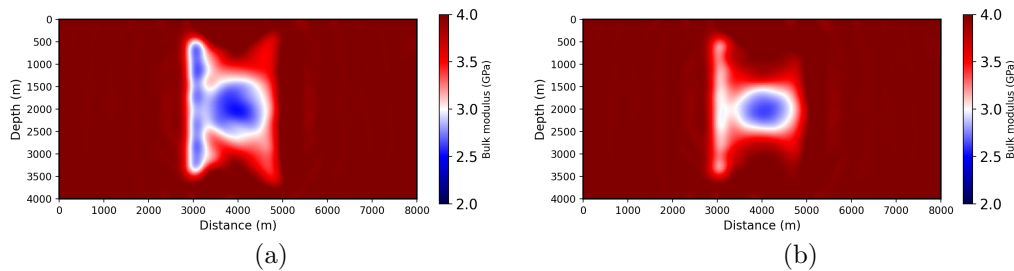


Figure 20: (a) Bulk modulus produced by 12 LBFSG steps to minimize the reduced MSWI objective using the data (one shot of which is) shown in 19. (b) Bulk modulus produced by 12 LBFSG steps to minimize the FWI objective starting at the MSWI result shown in Figure 20a.

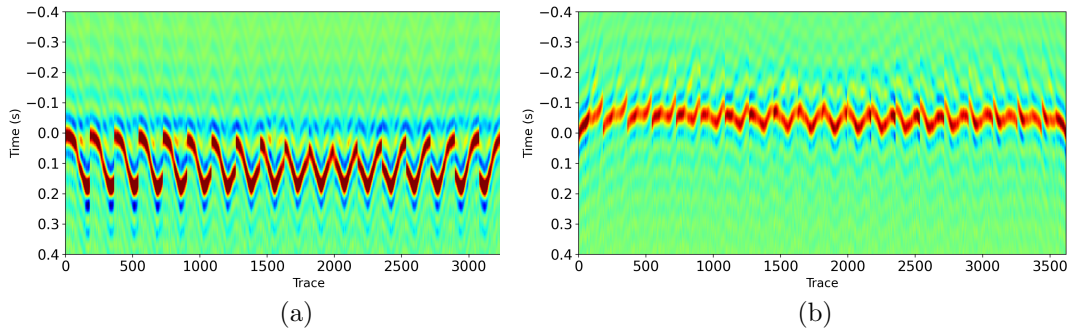


Figure 21: (a) Adaptive filter to match initial model data (Figure 2) to circular lens data with 32% added noise. (See Figure 19 for one shot of the noisy data.) Note considerable energy dispersion away from $t = 0$. (b) Adaptive filter to match data for MSWI model to noisy circular lens data. Note considerably less energy dispersion away from $t = 0$ than is evident in Figure 21a.

of wave physics.

FWI Failure Characterization

The FWI result shown in Figure 4 is certainly unsatisfactory, as is evident from the residual plot (Figure 3b). We found that a modest increase ($O(10)$) in the number of LBFGS iterations did not significantly improve the data fit. We cannot conclude from this observation that the model shown in Figure 4 is near a stationary point or local minimizer of the FWI objective function or that sufficiently many more iterations would not approximate a data-fitting model. However, even if orders of magnitude additional iterations *would* yield satisfactory data fit, such a vast amount of computational work is simply not practical. Nor is it sensible, since alternatives exist (FWI + MSWI) that accomplish the inversion goal with far less work. So, we don't know whether Figure 4 represents an approximation to a non-global local minimizer or not, but it doesn't matter.

Gradient Computation

The reader will note that the theory cited above shows that the MSWI objective function is close to the travel time mean square error under some circumstances. It does not however assert that the *gradients* of these two types of objective function are close. This omission prevents any theoretical conclusion about a relation between stationary points of MSWI and travel time tomography objective functions.

The computation of the gradient via the Variable Projection gradient formula 16 also requires a better theoretical foundation. The transpose-derivative DF^T of the modeling operator F tends to enhance high-frequency components of model perturbations, relative to the output of the modeling operator itself. In the case presented here and similar approaches, the field to which DF^T is applied is the result of iterative solution of a linear system, and the high frequency components of the iterates may not be assured to converge. In fact, the tangent approximation to this operator degrades in accuracy as maximum data frequency increases. The negative consequences of this phenomenon for accurate gradient computation, and possible fixes, have been discussed by several authors (see for example Symes (2015); Chauris and Farshad (2023)).

Choosing Penalty Parameters

The roles of parameters σ and α are quite different. Regularization, that is, avoidance of singularity in the normal equation 15, is the purpose of setting $\sigma > 0$. As formulated here, σ is a dimensional parameter. It is simple to make it dimensionless, and that should be done, so that a “small” choice is meaningful.

The penalty parameter α however plays a very different role. In principle, $\alpha \rightarrow \infty$ should force the adaptive filter to become “physical”, which in this case means the identity operator, i.e. with kernel $\delta(t)$ regardless of source and receiver, so that the penalty problem is identical to FWI. There are a variety of rules for setting penalty parameters like α . The discrepancy concept is one of these. It is simple to implement, doesn’t require a good initial value for problems like MSWI, and steers the penalty problem towards its limit. The trade off is this approach requires the assertion of data error. The penalty parameter α is adjusted so that the data error term in 9 is close to the posited size (see Fu and Symes (2017); Symes et al. (2022)). One might note that we have traded one difficult-to-estimate parameter (α) for another (data error). However it is possible to turn this construction around to estimate data error (Chen et al., 2022). In any case, data error has an obvious meaning, whether it is a known quantity or not, whereas α is merely a Lagrange multiplier.

Complex Wavefronts

As has been emphasized several times, wavefront complexity can prevent successful application of inversion methods based on source-receiver extension. The theoretical link between MSWI and similar methods, on the one hand, and travel time tomography, on the other, is broken in the presence of multiple ray paths between source and receiver, and numerical examples conform to the theory as already shown in the second oblate lens example (see also Symes (1994); Huang et al. (2017); Symes (2024)). However, the source-receiver extension is not the only possible route to FWI

modification by artificially expanding the definition of energy source. Huang et al. (2019) overview modifications of FWI based on various source extensions; some more recent advances are described by Métivier and Brossier (2020); Pladys et al. (2021); Li and Alkhalifah (2021); Yong et al. (2023); Operto et al. (2023); Symes (2023). Numerical examples suggest that some of these extensions may avoid cycle-skipping for transmitted wave data with complex wavefronts. For many of these approaches, the missing piece is a theoretical justification like that summarized in equations 10-13 for MSWI.

Applying MSWI to Other Types of Physics and Data

Acoustics is seldom exactly the right choice of physics for mechanical vibration modeling. In fact in many settings some variant of elastodynamics, perhaps coupled with acoustics in some regions, is the right choice. Elastic waves travel at several speeds, intrinsically providing multiple wavefronts. Extension of MSWI to elastodynamic inverse problems, either by data mode separation or some more intrinsic construction, would appear to be a very important next step, as would application to electromagnetic imaging.

Sensors (and energy sources) are seldom punctual and/or isotropic. Actual sources encountered in lab and field experiments can exhibit non-trivial radiation patterns or even a physical extent which is non-negligible on the wavelength scale. Inclusion of more realistic source modeling also seems a very important next step for testing the limits of source-receiver extension.

Finally, the assumption of smooth material parameter variation is unlikely to be justified in actual physical media. Sedimentary rocks, human tissue, and manufactured objects all exhibit juxtaposition of structure at all scales, from long scales modeled by smooth variation, to sub-wavelength oscillations. Most likely in settings where ballistic transmitted waves dominate the data energetics, techniques like MSWI can be applied to gain a low-resolution image of model parameters like wave velocity or bulk modulus, etc. However theoretical results in this direction are absent, as are results on the related question of applicability of algorithms like MSWI to predominantly reflected wave data.

CONCLUSIONS

Matched Source Waveform Inversion is one of several extension methods that can avoid the cycle skipping phenomenon afflicting standard least-squares (full waveform) inversion in certain special cases. The adaptive filter in MSWI helps align the predicted and observed data, which allows for larger model adjustments than can be made using local-gradient based optimization on the FWI objective. In this paper

we provide a catalogue of numerical experiments that illustrate several features of MSWI. All of these experiments use relatively simple (and similar) heterogeneous velocity models with a single anomaly embedded within a homogeneous background medium. They all assume a single vertical line of sources on the left of the anomaly and another vertical line of receivers on the right. Despite their simplicity, these velocity models illustrate how and when MSWI can provide a good starting model for FWI. In a related theory paper, MSWI applied to single-arrival data is shown to be equivalent to travel-time tomography which does not suffer from cycle skipping. We first show an experiment with single arrival data that illustrates failure of FWI to converge to a reasonable velocity when the inversion is started from a homogeneous initial model. MSWI, on the other hand, succeeds for this same experiment. Further, this MSWI result can be used as an initial guess for FWI allowing further refinement of the model. However, when the model and acquisition geometry of the experiment change so that the data includes multiple arrivals, our numerical examples indicate that MSWI is no longer able to find a reasonable velocity from a homogeneous initial model. Additionally we show that with moderate levels of added noise, MSWI is still able to converge to a reasonable velocity model from a homogeneous starting model.

ACKNOWLEDGEMENTS

The authors gratefully acknowledge support from the sponsors of the UT Dallas *3D+4D Seismic FWI* research consortium.

REFERENCES

- Barnier, G., E. Biondi, R. Clapp, and B. Biondi, 2023a, Full-waveform inversion by model extension: Practical applications: *Geophysics*, **88**, R609–R643.
- , 2023b, Full-waveform inversion by model extension: Theory, design, and optimization: *Geophysics*, **88**, R579–R607.
- Bording, R., A. Gersztenkorn, L. Lines, J. Scales, and T. S., 1987, Applications of seismic travel-time tomography: *Geophysical Journal International*, **90**, 285–303. (<https://doi.org/10.1111/j.1365-246X.1987.tb00728.x>).
- Chauris, H., and M. Farshad, 2023, Seismic differential semblance-oriented migration velocity analysis — status and the way forward: *Geophysics*, **88**, U81–U100.
- Chavent, G., and P. Lemmonier, 1974, Identification de la non-linéarité d’une équation parabolique quasilinéaire: *Applied Mathematics and Optimization*, **1**, 121–162.
- Chen, H., W. Symes, and S. Minkoff, 2022, Use of extended source inversion for estimating the noise level in seismic data: *Second International Meeting for Applied Geoscience and Energy, Expanded Abstracts, Society of Exploration Geophysicists*, 887–891.
- Cohen, G. C., 2002, *Higher order numerical methods for transient wave equations*: Springer.

- Daniels, J., 1967, The conjugate gradient method for linear and nonlinear operator equations: *SIAM Journal on Numerical Analysis*, **4**, 10–26.
- Fu, L., and W. W. Symes, 2017, A discrepancy-based penalty method for extended waveform inversion: *Geophysics*, **82**, no. 5, R287–R298.
- Gauthier, O., A. Tarantola, and J. Virieux, 1986, Two-dimensional nonlinear inversion of seismic waveforms: *Geophysics*, **51**, 1387–1403.
- Golub, G., and V. Pereyra, 1973, The differentiation of pseudoinverses and nonlinear least squares problems whose variables separate: *SIAM Journal on Numerical Analysis*, **10**, 413–432.
- , 2003, Separable nonlinear least squares: the variable projection method and its applications: *Inverse Problems*, **19**, R1–R26.
- Griewank, A., 1992, Achieving logarithmic growth of temporal and spatial complexity in reverse automatic differentiation: *Optimization Methods and Software*, **1**, 35–54.
- , 2000, *Evaluating derivatives: Principles and techniques of algorithmic differentiation*: Society for Industrial and Applied Mathematics (Frontiers in Applied Mathematics 19).
- Guasch, L., A. Calderón, M. Tang, P. Nachev, and M. Warner, 2020, Full-waveform inversion imaging of the human brain: *NPJ Digital Medicine*, **3**.
- Guasch, L., M. Warner, and C. Ravaut, 2019, Adaptive waveform inversion: *Practice: Geophysics*, **84**, R447–R461.
- Huang, G., R. Nammour, and W. Symes, 2017, Full waveform inversion via matched source extension: *Geophysics*, **82**, R153–R171.
- Huang, G., R. Nammour, W. Symes, and M. Dolliazal, 2019, Waveform inversion by source extension: 89th Annual International Meeting, Expanded Abstracts, Society of Exploration Geophysicists, 4761–4765.
- Huang, G., and W. W. Symes, 2015, Full waveform inversion via matched source extension: 85th Annual International Meeting, Expanded Abstracts, Society of Exploration Geophysicists, 1320–1325.
- Kaufman, L., 1975, A variable projection method for solving separable nonlinear least squares problems: *BIT: Numerical Mathematics*, **15**, 49–57.
- Kavand, A., and M. Bekrani, 2024, Speckle noise removal in medical ultrasonic image using spatial filters and dncnn: *Multimedial Tools and Applications*, **83**, 45903–45920. (<https://doi.org/10.1007/s11042-023-17374-7>).
- Levander, A. R., 1988, Fourth-order finite-difference P-SV seismograms: *Geophysics*, **53**, 1425–1436.
- Li, Y., and T. Alkhalifah, 2021, Extended full waveform inversion with matching filter: *Geophysical Prospecting*, **69**, 1441–1454.
- Luo, S., and P. Sava, 2011, A deconvolution-based objective function for wave-equation inversion: 81st Annual International Meeting, Expanded Abstracts, Society of Exploration Geophysicists, 2788–2792.
- Métivier, L., and R. Brossier, 2020, A receiver-extension approach to robust full waveform inversion: 90th Annual International Meeting, Expanded Abstracts, Society of Exploration Geophysicists, 641–645.
- Mukhometov, R., 1975, The inverse kinematic problem of seismology on the plane: *Mathematical Problems of Geophysics*, Akad. Nauk. SSSR, **6**, 243–52. ((in Rus-

- sian)).
- Nocedal, J., and S. Wright, 1999, Numerical Optimization: Springer Verlag.
- Operto, S., A. Gholami, H. Aghamiry, G. Guo, S. Beller, K. Aghazade, F. Mamboumbi, L. Combe, and A. Ribodetti, 2023, Extending the search space of full-waveform inversion beyond the single-scattering born approximation: A tutorial review: *Geophysics*, **88**, R671–R702.
- Pladys, A., R. Brossier, Y. Li, and L. Métivier, 2021, On cycle-skipping and misfit function modification for full-wave inversion: Comparison of five recent approaches: *Geophysics*, **86**, R563–R587.
- Plessix, R.-E., 2000, Automatic cross-well tomography: an application of the differential semblance optimization to two real examples: *Geophysical Prospecting*, **48**, 937–951.
- Shearer, P. M., 2009, Introduction to seismology: Cambridge University Press.
- Sirgue, L., and G. Pratt, 2004, Efficient waveform inversion and imaging: a strategy for selecting temporal frequencies: *Geophysics*, **69**, 231–248.
- Song, H., 1994, On a transmission inverse problem: PhD thesis, Computational and Applied Mathematics Department, Rice University, Houston, Texas, U.S.A.
- Steihaug, T., 1983, The conjugate gradient method and trust regions in large scale optimization: *SIAM Journal on Numerical Analysis*, **20**, 626–637.
- Symes, W., 1994, Inverting waveforms in the presence of caustics: Technical report, The Rice Inversion Project. (<http://wwsorcas.com/reports/1994/report.html>).
- , 2007, Reverse time migration with optimal checkpointing: *Geophysics*, **72**, SM213–222.
- , 2015, Algorithmic aspects of extended waveform inversion: 76th Annual International Conference and Exhibition, Expanded Abstracts, European Association of Geoscientists and Engineers, WS05–A01.
- , 2023, Efficient computation of extended surface sources: *International Journal on Geomathematics*, **14**, 3.
- , 2024, Adaptive waveform inversion for transmitted wave data. (arXiv:2402.17696).
- Symes, W., H. Chen, and S. Minkoff, 2022, Solution of an acoustic transmission inverse problem by extended inversion: *Inverse Problems*, **38**, 115003.
- Symes, W., D. Sun, and M. Enriquez, 2011, From modelling to inversion: designing a well-adapted simulator: *Geophysical Prospecting*, **59**, 814–833. (DOI:10.1111/j.1365-2478.2011.00977.x).
- Tarikere, A., and H. Zhou, 2024, Stability and statistical inversion of travel time tomography: *Inverse Problems*, **40**, 075003.
- Virieux, J., 1986, P-SV wave propagation in heterogeneous media: Velocity-stress finite-difference method: *Geophysics*, **51**, 889–901.
- Virieux, J., and S. Operto, 2009, An overview of full waveform inversion in exploration geophysics: *Geophysics*, **74**, no. 6, WCC127–WCC152.
- Warner, M., and L. Guasch, 2016, Adaptive waveform inversion: theory: *Geophysics*, **81**, R429–R445.
- Warner, M., T. Nangoo, A. Umpleby, N. Shah, D. Kahn, and M. Isernia, 2021, Adaptive reflection waveform inversion: Faster, tighter, deeper, smarter: 91st Annual

International Meeting, Expanded Abstracts, Society of Exploration Geophysicists, 582–586.

Yong, P., R. Brossier, L. Métivier, and J. Virieux, 2023, Localized adaptive waveform inversion: theory and numerical verification: *Geophysical Journal International*, **233**, 1055–1080.

Zhu, C., R. H. Byrd, and J. Nocedal, 1997, L-BFGS-B, FORTRAN routines for large scale bound constrained optimization: *ACM Transactions on Mathematical Software*, **23**, 550–560.